Energy Advances

ROYAL SOCIETY OF CHEMISTRY

PAPER

View Article Online
View Journal | View Issue



Cite this: *Energy Adv.*, 2023, 2, 556

# Band structure engineering of a polyimide photocatalyst towards enhanced water splitting†

Sheng Chu, [abc] Xintie Wang,[a] Liu Yang,[a] Huiyan Zhang, *[a] Rui Xiao,[a] Ying Wang *[bc] and Zhigang Zou[c]

Received 19th January 2023,
Accepted 13th March 2023

DOI: 10.1039/d3ya00038a

rsc.li/energy-advances

Polyimide (PI), a typical donor–acceptor polymeric semiconductor, exhibits promising photocatalytic applications owing to its distinct advantages of facile synthesis, easy functionalization and molecularly tunable optoelectronic properties. However, PI in its pristine form has moderate photocatalytic activity due to non-optimal band structure and fast recombination of photo-excited charge carriers. Herein, we report the band structure engineering of PI for enhanced photocatalytic water splitting by simply tuning the feed ratio of the amine and anhydride monomer. Anhydride-rich PI possesses lower valence band position and stronger photooxidation capability, resulting in a preferential activity for water oxidation over water reduction in comparison with amine-rich PI. The structure–activity relationships revealed in this work shed light on the rational design of polymeric photocatalysts with suitable redox energetics for specific photoreactions.



## 1. Introduction

Solar-powered photocatalytic water splitting into hydrogen has been considered a green and sustainable approach to convert intermittent solar energy into storable chemical fuel.[1–6] In the solar-to-fuel conversion process, a semiconductor photocatalyst plays an essential role. Recently, substantial research efforts have been devoted to organic polymers such as graphic carbon nitride (g-$C_3N_4$),[7–15] covalent organic frameworks (COFs),[16–20] covalent triazine-based frameworks (CTFs),[21–25] and conjugated microporous polymer (CMPs),[26–29] due to their easily regulated electron band structure, high physicochemical stability, low cost and ease of synthesis from earth-abundant sources. Among polymeric photocatalysts, polyimide (PI), a polymer with a typical binary donor–acceptor (D–A) structure was demonstrated to have photocatalytic $H_2$ evolution capability in 2012.[30] PI can be prepared by simple green thermal condensation of electron-rich amines and electron-deficient dianhydride monomers at mild temperatures below 350 °C.[31] The D–A structure of PI endows it with diverse synthetic chemistry and is beneficial for effective electron–hole separation and transfer.[27] However, the photocatalytic efficiency of pristine PI is still moderate because of the severe photogenerated charge recombination, unfavorable electronic band structure and poor surface reaction kinetics. To increase the photocatalytic efficiency, a number of different approaches have been investigated to date, such as doping,[32–34] co-monomer tuning,[35–39] morphology engineering,[40–42] and composite structure design.[43–49]

The most fundamental property of a semiconductor photocatalyst that directly affects its photocatalytic performance is its band structure.[50–52] Ideally, the photocatalyst requires a combination of a suitable band gap for sunlight absorption and appropriate band positions to be consistent with the water splitting redox potentials. Theoretically, the valence band (VB) position of a semiconductor should be lower than the redox potential of $O_2/H_2O$, and the conduction band (CB) position should be higher than the redox potential of $H^+/H_2$ as required by thermodynamics. Water oxidation, one of the two half-reactions in water splitting, has sluggish reaction kinetics of four-electron transfer processes involving the formation of O–O bonds and the cleavage of O–H bonds, which often limits the overall water splitting performance.[52–55] Therefore, it is important to modulate the band positions to enhance the photooxidation strength for water oxidation.

As for the D–A polymer photocatalyst, an effective strategy to precisely tune the band structure is to vary the compositions of electron-donating or electron-accepting components.[56–59] For example, for the purpose of photocatalytic oxygen evolution, Wang and colleagues altered the band structure of conjugated

[a] *Key Laboratory of Energy Thermal Conversion and Control of Ministry of Education, School of Energy and Environment, Southeast University, Nanjing 210096, P. R. China. E-mail: hyzhang@seu.edu.cn*
[b] *School of Chemistry and Chemical Engineering, Nanjing University, Nanjing 210023, P. R. China. E-mail: wangy@nju.edu.cn*
[c] *Eco-materials and Renewable Energy Research Center (ERERC), National Laboratory of Solid State Microstructures, Kunshan Innovation Institute of Nanjing University, Jiangsu Key Laboratory for Nanotechnology, Nanjing University, Nanjing 210023, P. R. China*

† Electronic supplementary information (ESI) available. See DOI: https://doi.org/10.1039/d3ya00038a

triazine-based polymers (CTPs).[60] By increasing the number of benzyl units in the backbone that donate electrons, the electronic, optical, and redox properties of CTPs were finely adjusted, thereby improving the photocatalytic oxygen evolution performance. In another example, Zhang and colleagues reported on a cluster of D–A organic semiconductors by altering the combination of electron donor and acceptor in the molecular structure.[61] The redox potentials of the photocatalyst were finely controlled to achieve optimum photocatalytic performance in the intermolecular C–H functionalization. Very recently, Liu and co-workers constructed an effective D–A conjugated polymer photocatalyst for $CO_2$ reduction by choosing appropriate monomers with the guidance of theoretical analysis of molecular orbital energies.[62] Based on these previous findings, we intend to improve PI's molecular structure so that it can be used effectively for water splitting, which remains largely unexplored. Herein, we modulate the band structure of PI through simply varying the content of the electron-donor and -acceptor moieties in the polymer skeleton. The influence of band structure on the photocatalytic water splitting performance was investigated, and theoretical calculations were combined to clarify the connection between structure and activity.

## 2. Material and methods

### 2.1 Sample synthesis

Melamine (MA) and pyromellitic dianhydride (PMDA) were purchased from Shanghai Lingfeng Chemical Reagent Co., Ltd. and TCI Shanghai Chemical Reagent Co., Ltd, respectively. PI samples were prepared as described in the previous report.[30] MA and PMDA were mixed uniformly with a particular molar ratio (1 : 1 and 1 : 2 for **AM-PI** and **AD-PI**, respectively) and transferred into a porcelain crucible. The mixture was then put into a muffle furnace, where it was heated for 4 h at a rate of 7 °C $min^{-1}$ to 325 °C. After washing with acetone and water, the powder was dried in an oven to produce the resultant sample.

### 2.2 Sample characterization

Fourier transform infrared (FT-IR) spectra were conducted on a Nicolet NEXUS870 spectrometer. Element analysis (EA) tests were performed on an Elementar Vario EL and calibrated by analytically pure MA as a nitrogen standard. X-ray diffraction (XRD) analysis was tested on a Rigaku Ultima III X-ray diffractometer with Cu Kα radiation. The UV-Vis absorbance spectra were collected on a Shimadzu UV-2550 spectrometer. The valence band X-ray photoelectron spectra (VBXPS) were performed on a PHI 5000 Versa Probe photoelectron spectrometer with Al Kα radiation. The steady and time-resolved photoluminescence spectra (PL) were recorded on an Edinburgh FLS1000 fluorescence spectrometer. The electron spin resonance (ESR) spectra were collected on a Bruker EMXplus-6/1 spectrometer.

### 2.3 Photocatalytic test

Photocatalytic tests were conducted in a closed gas circulation system, including hydrogen and oxygen evolution half-reactions of water splitting. A 300 W xenon lamp equipped with a 420 nm cutoff filter was used as the visible light source. The reaction temperature was maintained at 10 °C by a circulating water system. The system was evacuated multiple times to remove air before the reaction. In the $H_2$ evolution reaction, 0.2 g of sample was dispersed in 360 ml of water and 40 ml of methanol was added as a hole scavenger. Before $H_2$ evolution, 1 wt% Pt was used as the cocatalyst through the photo-deposition method by using $H_2PtCl_6$ dissolved in the reaction solution. The solution was irradiated under a xenon lamp without a filter for 1 h to promote the photodeposition of Pt. Subsequently, the system was evacuated again and $H_2$ evolution reaction was carried out under visible light. The reaction of $O_2$ evolution was similar to the $H_2$ evolution reaction, except that 0.2 g photocatalyst was dispersed in 400 ml of water with 0.01 M $AgNO_3$ as an electron scavenger and 0.4 g $La_2O_3$ as pH buffer. The amount of produced gas was quantified by online gas chromatography (GC-14C, Shimadzu, TCD, Ar carrier).

### 2.4 DFT calculations

The Gaussian 03 program was used for molecular calculations and the B3LYP/6-31g method was used for optimization. Based on the optimization results, the highest occupied molecular orbital (HOMO) and the lowest unoccupied molecular orbital (LUMO) were displayed in the Gview program.

## 3. Results and discussion

### 3.1 Synthesis and structural characterization

A facile thermal condensation method was used to synthesize the PI photocatalyst according to the previous work.[30] Two PIs, denoted as **AM-PI** and **AD-PI**, were prepared by co-polymerizing MA and PMDA at 325 °C with a molar ratio of 1 : 1 and 1 : 2, respectively (Scheme 1). The mild reaction conditions are attributed to the crystalline PI products with high yield over 95%. To confirm the successful synthesis of **AM-PI** and **AD-PI**, FTIR, EA and XRD analyses were conducted. As shown in the FTIR spectra (Fig. 1), in five-membered imide rings, the vibrations of asymmetric stretching, symmetric stretching, and bending of C=O are represented by the bands around 1772, 1720, and 725 $cm^{-1}$. In the imide rings, the vibration of C–N–C stretching is represented by the band at 1381 $cm^{-1}$.[31] These characteristic peaks indicate the formation of a typical polyimide structure. Besides, the characteristic peaks of **AM-PI** and **AD-PI** differ in a few ways. In the **AM-PI** sample, the three peaks above 3300 $cm^{-1}$ and the peak at 1640 $cm^{-1}$ indicate the N–H stretching and bending vibration of terminal amino groups, respectively, while a peak at 1851 $cm^{-1}$ indicates the C=O stretching vibration of terminal anhydride groups in the AD-PI (**http://AD-PI**) sample.[63] As expected, no characteristic absorption peaks of anhydride group and amino group were detected in **AM-PI** and **AD-PI**, respectively, indicating the synthesis of anhydride-terminated and amino-terminated PI. Furthermore, the band at 1670 $cm^{-1}$ of the amine–acid intermediate was not

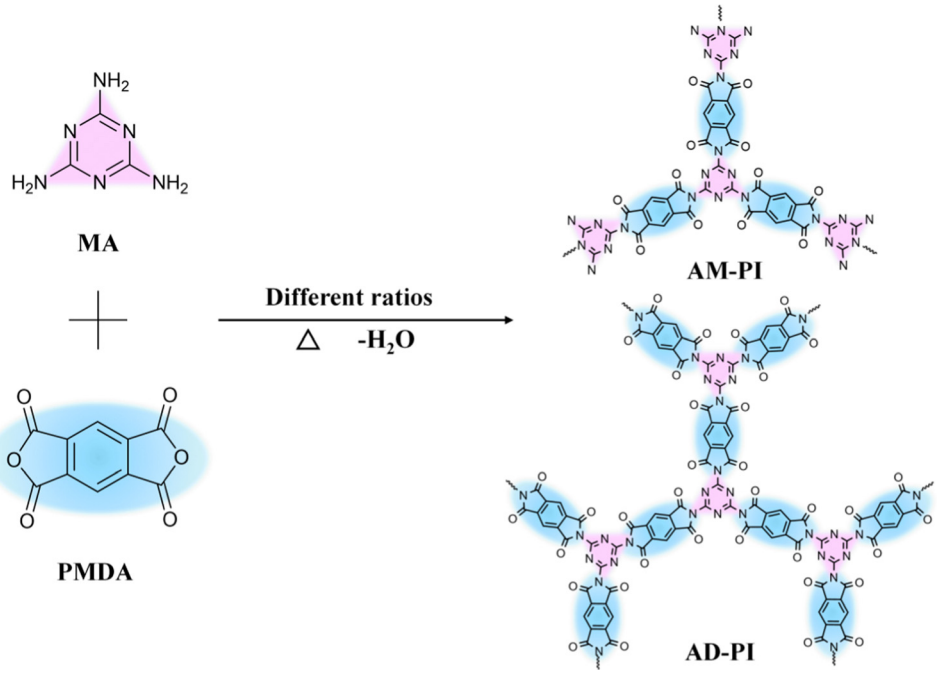


Scheme 1 Reaction scheme for the synthesis of **AM-PI** and **AD-PI**.

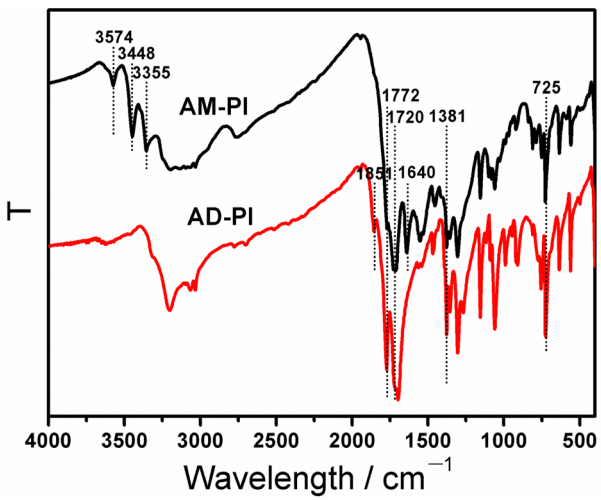


Fig. 1 FTIR spectra of **AM-PI** and **AD-PI**.

detected in **AM-PI** and **AD-PI**, indicating that the imidization reaction was complete.[30]

To further confirm the chemical structure of **AM-PI** and **AD-PI**, the elemental composition was analyzed (Table 1). It was found that the experimental values of the C, H, O and N contents of **AM-PI** and **AD-PI** are close to the theoretical values, indicating that the presumed PI was synthesized. **AM-PI** has a significantly higher nitrogen content than **AD-PI** because of its amino-rich moiety. Similarly, **AD-PI** is rich in anhydride moiety and has much higher oxygen content than **AM-PI**. An XRD test was performed to investigate the stacking structure of the samples. As shown in Fig. 2, by comparing the XRD patterns

Table 1 Elemental analysis and theoretical results of **AM-PI** and **AD-PI**

| Element (wt%) | C | H | N | O |
|---|---|---|---|---|
| **AM-PI** (experimental) | 49.52 | 2.20 | 28.70 | 19.58 |
| **AM-PI** (theoretical, $C_{13}H_4N_6O_4$) | 50.66 | 1.31 | 27.27 | 20.76 |
| **AD-PI** (experimental) | 53.33 | 1.47 | 17.05 | 28.15 |
| **AD-PI** (theoretical, $C_{23}H_4N_6O_9$) | 54.33 | 0.79 | 16.54 | 28.35 |

of the PI and the reaction monomers, no residual peak of the MA or PMDA was detected, indicating that the reaction was complete and no precursor was left in the samples. The XRD patterns of PI coincided with that in the literature.[30,31] Both

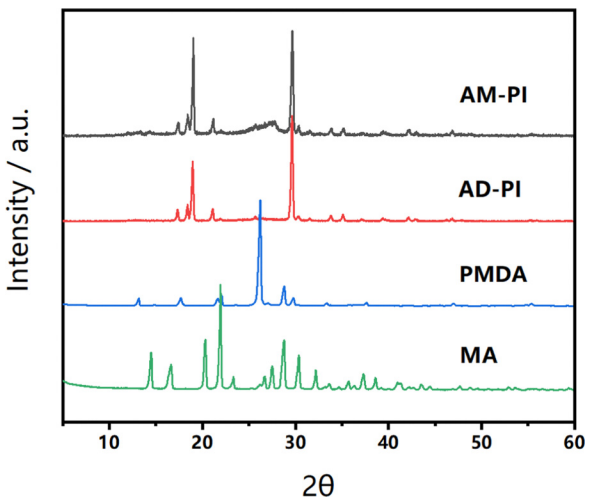


Fig. 2 XRD patterns of **AM-PI**, **AD-PI**, PMDA and MA.

**AM-PI** and **AD-PI** showed high crystallization with similar peak positions, indicating the same arrangement of chain structures. However, **AD-PI** has a significantly stronger peak intensity than **AM-PI**, indicating its more ordered chain arrangement. This may be related to the solid-phase thermal polymerization process. PMDA is in a molten state during the polymerization process, and the PI product is crystallized from the monomer melt.[25] When the proportion of PMDA melt is higher, the π–π electron interactions between PI chains are stronger, which is conducive to forming a more regular chain orientation.

### 3.2 Optical and electronic properties

In order to investigate the band energy structures of the PI samples, their electronic as well as optical properties were investigated. The results of UV-Vis diffuse reflectance spectra of **AM-PI** and **AD-PI** indicated their effective adsorption capacity in the visible light range (Fig. 3). According to the Kubelka–Munk formula $E_g$ (eV) = 1240/$\lambda$ (nm), the calculated **AM-PI** and **AD-PI** band gaps are 2.76 and 2.88 eV, respectively. The different band gaps can be ascribed to the different proportions of amine and anhydride monomers. However, it cannot be excluded that the polymerization degree and fragment size also affect the energy band gap of PI. Besides, VBXPS was conducted to investigate the VB position of the PI samples. As depicted in Fig. 4, the VB values of **AM-PI** and **AD-PI** were estimated to be 1.01 and 1.78 eV, respectively. Consequently, the optical band gaps and VB positions are used to determine the CB positions of **AM-PI** and **AD-PI**, and the band structures of the PI samples are displayed in Fig. 5. Both the CB and VB positions of **AD-PI** locate lower than that of **AM-PI**. The lower VB position of **AD-PI** indicates that it has a higher photooxidation ability, which can be attributed to the more content of electron-withdrawing anhydride components in the backbone and edge of the catalyst.[64,65]

To acquire a comprehensive understanding of band structure modulation, DFT calculations of PI cluster models were performed (Fig. 6). It was found that the HOMO and LUMO of **AD-PI** are both downshifted compared to **AM-PI**, which is consistent with the experimental results. This is not unexpected since the oxygen atom in the anhydride moiety is more electronegative than nitrogen (3.44 *vs.* 3.04). In addition, the DFT calculations of the HOMO and LUMO positions of the **AM-PI** and **AD-PI** models indicate similar distributions: the HOMO and LUMO are situated in the MA moiety and PMDA moiety, respectively (Fig. 7). The spatial separation of the HOMO and LUMO positions benefits the charge carrier separation as well as migration, which is advantageous for the photocatalytic performance.[64,66,67] It is worth noting that the calculated energy band values differ from the experimental observations, because the PI model used in the DFT calculations is a simplified small molecule, and the model does not consider the interactions between molecular chains.

PL spectra were measured to reveal their difference in the photogenerated electron transfer. From Fig. S1a (ESI†), the intensity of **AD-PI** is higher than that of **AM-PI**, indicating that

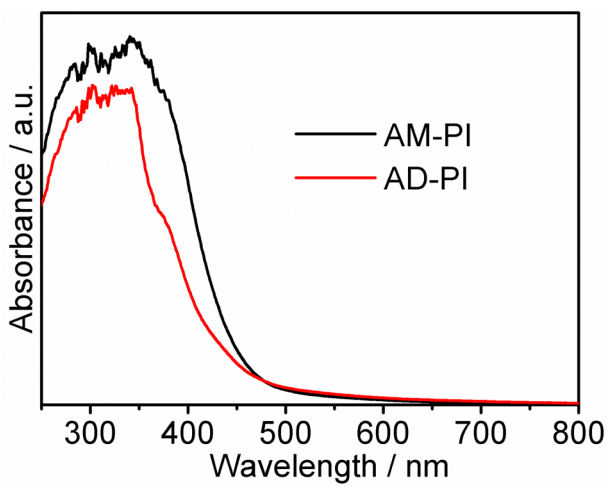


Fig. 3 UV-Vis absorption spectra of **AM-PI** and **AD-PI**.

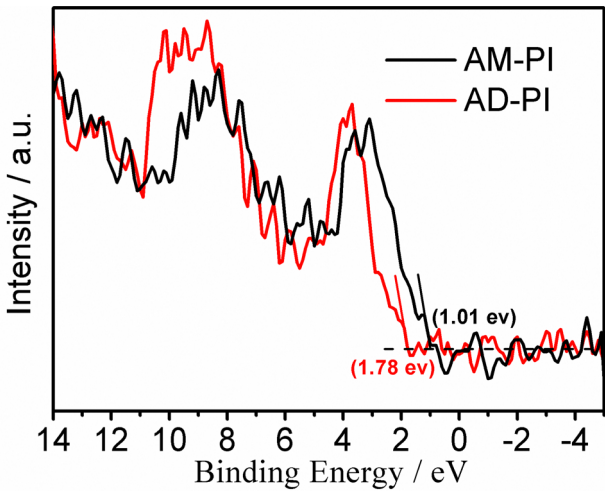


Fig. 4 VBXPS of **AM-PI** and **AD-PI**.

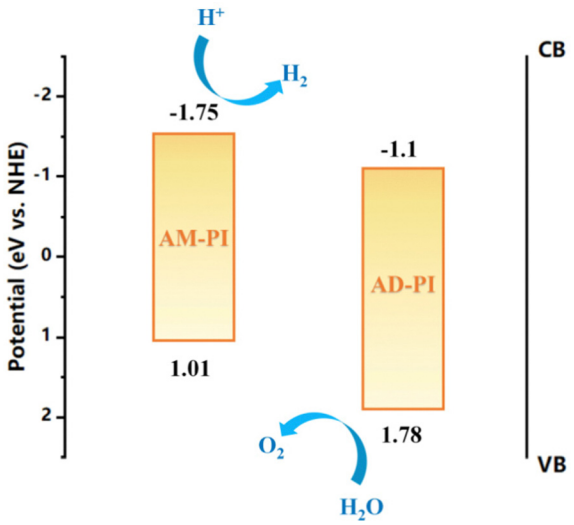


Fig. 5 Band structures of **AM-PI** and **AD-PI**.

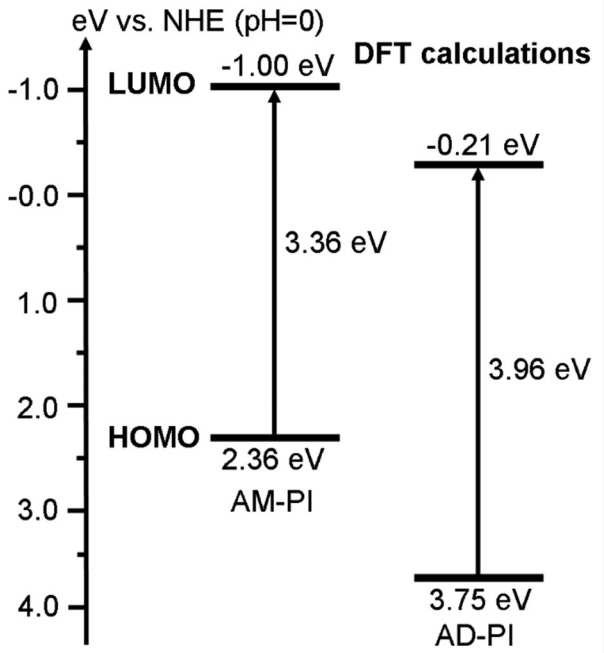


Fig. 6 DFT calculated HOMO and LUMO energy levels of the optimized **AM-PI** and **AD-PI** models.

the recombination of photoexcited charge carriers was suppressed in **AM-PI**. The rapid electron-hole recombination in **AD-PI** might be due to the stronger π–π intermolecular interaction, which can accelerate the mobility of the charge carriers.[35,68] Furthermore, ESP spectra were performed to study the delocalization of π electrons. The tests were carried out in the dark and under visible light at 10 min. As shown in Fig. S1b (ESI†), all the samples show a Lorentzian line at $g$ = 2.000; however, the signal intensity is different due to the different D/A ratios in PI. After light illumination, the intensity of **AD-PI** increased significantly, while **AM-PI** increased slightly. This indicates that the electrons are much easier to excite on **AD-PI** to give photogenerated electron/hole pairs under visible light irradiation. Therefore, the photogenerated carriers' separation and transfer ability of **AD-PI** were higher than that of **AM-PI** due to its excellent electron delocalization property and strong π–π intermolecular interactions, which is consistent with the results of PL.[35,69]

### 3.3 Photocatalytic properties

Under visible light irradiation (>420 nm), two half-reactions of photocatalytic water splitting were used as probes to investigate the photocatalytic performance of **AM-PI** and **AD-PI**. In the hydrogen evolution half reaction, Pt (1 wt%) was loaded as the cocatalyst while methanol (10 vol%) was used as a sacrificial agent to consume holes. In the blank test, the reaction did not occur under dark conditions, indicating that light was indispensable. As depicted in Fig. 8(a), the hydrogen evolution rate of **AM-PI** (15.2 μmol $h^{-1}$) was 3.8-fold higher than that of **AD-PI** (4.0 μmol $h^{-1}$), which can be ascribed to the higher CB position, narrowed band gap and larger surface area of **AM-PI** compared to **AD-PI** (5.1 *vs.* 1.9 $m^2$ $g^{-1}$). In contrast, a completely opposite trend was found in the photocatalytic oxygen evolution reaction, when $AgNO_3$ was added as the electron sacrificial

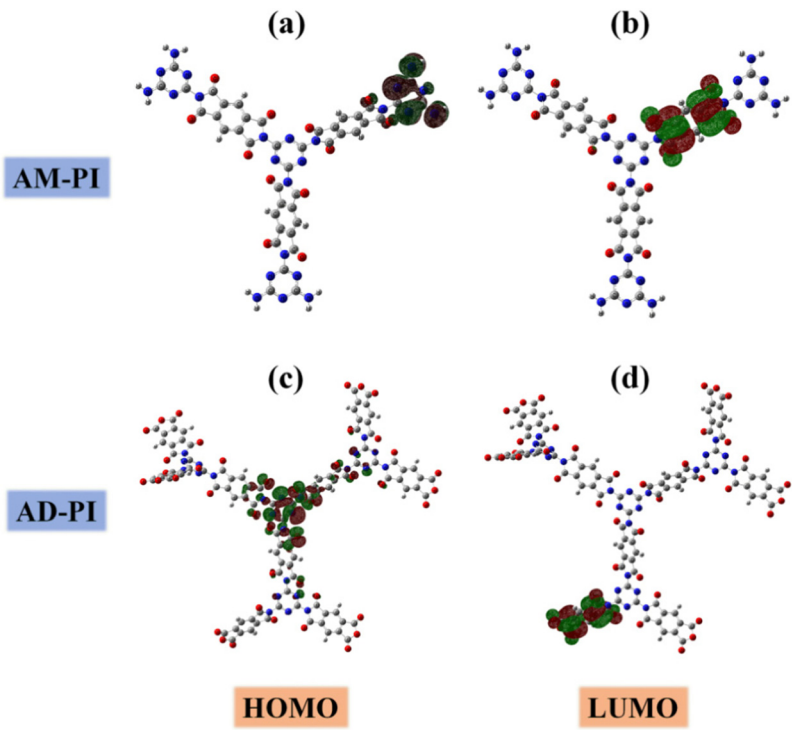


Fig. 7 (a) HOMO and (b) LUMO of the geometry-optimized AM-PI model; (c) HOMO and (d) LUMO of the geometry-optimized AD-PI model.

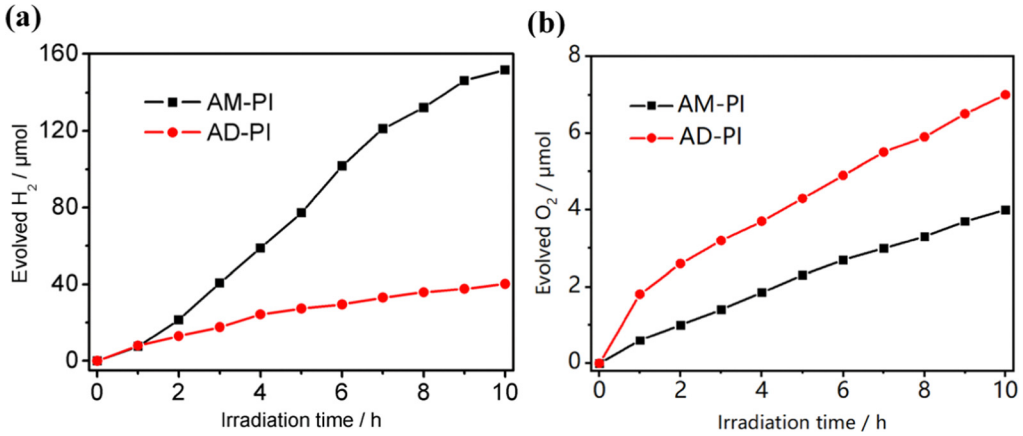


Fig. 8 Time course of (a) $H_2$ evolution from a 10 vol% aqueous methanol solution by 1 wt% Pt-deposited PI samples and (b) $O_2$ evolution from a 0.01 M aqueous $AgNO_3$ solution by bare PI samples. Reaction conditions: 100 mg of PI, visible light irradiation ($\lambda > 420$ nm).

agent. The oxygen evolution rate of **AD-PI** was 0.7 μmol $h^{-1}$ (Fig. 8(b)), which was far higher than that of **AM-PI** (0.4 μmol $h^{-1}$). In addition, we also calculated the specific activity of hydrogen evolution and oxygen evolution; as shown in Table S1 (ESI†), the specific activity of the hydrogen evolution rate of **AM-PI** was 1.4-fold higher than that of **AD-PI**, and the oxygen evolution rate of **AD-PI** was 4.6-fold higher than that of **AM-PI**, which also supports the above conclusion. Compared with **AM-PI**, the VB position of **AD-PI** was greatly reduced by about 0.77 V, resulting in a significantly enhanced photooxidation capability and thus $O_2$ evolving activity. Therefore, band structure modulation of PI plays a critical role in controlling the photocatalytic oxidation and reduction performance. In order to eliminate the possible reactivity from reactive monomers, MA and PMDA were heated separately at 325 °C to obtain MA-325 and PMDA-325, which were found to have no activity in the hydrogen and oxygen evolution experiments. In addition, we carried out FTIR and XRD characterizations on the monomer samples and found that the structure of the two samples did not change after heating solely (Fig. S2, ESI†). Therefore, it can be determined that the hydrogen and oxygen evolution activities were generated by PI.

The catalyst stability tests of the PI samples were also performed. After four cycles, the hydrogen evolution rate of **AM-PI** did not decrease obviously (Fig. S3, ESI†). As shown in Fig. S4 (ESI†), the FTIR and XRD signals of **AM-PI** after the hydrogen evolution cycle experiment are almost the same as before. In oxygen evolution cycle experiments, the oxygen evolution rate of **AD-PI** decreased significantly from 0.7 μmol $h^{-1}$ to 0.3 μmol $h^{-1}$ in the second run. This can be ascribed to the deposition of Ag nanoparticles on the surface of the PI catalyst (generated from the photoreduction of $Ag^+$), which leads to a light shading effect and hinders optical absorption. The hydrogen and oxygen evolution activities reported in this work are comparable with the reported values of PI in the literature (Table S2, ESI†). However, the performance of hydrogen and oxygen evolution can be further improved, considering the large band gaps of **AM-PI** (2.76 eV) and **AD-PI** (2.88 eV) resulting in limited visible light absorption. In the subsequent work, the band gap of PI can be optimized by tuning the polymerization temperature and co-monomer structure.

## 4. Conclusion

In summary, we demonstrate the band structure regulation of PI by simply adjusting the feed ratio of amine and anhydride monomer. Compared with amine-rich PI, anhydride-rich PI possesses lower valence band position and stronger photooxidation capability due to the electron-withdrawing property of the anhydride constituent, leading to a preferential photoactivity for water oxidation over water reduction. This work opens new opportunities on the rational design of polymer photocatalysts with suitable energy band structure for enhanced photocatalytic performance.

## Conflicts of interest

The authors declare that they have no known competing financial interests or personal relationships that could have appeared to influence the work reported in this paper.

## Acknowledgements

This work was supported by the Scientific and Technological Innovation Project of Carbon Emission Peak and Carbon Neutrality of Jiangsu Province (BE2022028-4), the National Natural Science Foundation of China (22005048, 22179060) and the Natural Science Foundation of Jiangsu Province (grants no. BK20200399). Sheng Chu would like to acknowledge the support from the ''Zhishan Young Scholar'' Program of Southeast University.

## References


1 A. Kudo and Y. Miseki, Heterogeneous photocatalyst materials for water splitting, *Chem. Soc. Rev.*, 2009, **38**, 253–278.
2 X. B. Chen, S. H. Shen, L. J. Guo and S. S. Mao, Semiconductor-based photocatalytic hydrogen generation, *Chem. Rev.*, 2010, **110**, 6503–6570.
3 X. P. Tao, Y. Zhao, S. Y. Wang, C. Li and R. G. Li, Recent advances and perspectives for solar-driven water splitting using particulate photocatalysts, *Chem. Soc. Rev.*, 2022, **51**, 3561–3608.
4 S. Chu, W. Li, Y. F. Yan, T. Hamann, I. Shih, D. W. Wang and Z. T. Mi, Roadmap on solar water splitting: current status and future prospects, *Nano Futures*, 2017, **1**, 022001.
5 Pratibha, A. Kapoor and J. K. Rajput, Nanostructured materials for the visible-light driven hydrogen evolution by water splitting: A review, *Int. J. Hydrogen Energy*, 2022, **47**, 17544–17582.
6 N. Pirrone, F. Bella and S. Hernandez, Solar $H_2$ production systems: current status and prospective applications, *Green Chem.*, 2022, **24**, 5379–5402.
7 A. Akhundi, A. Badiei, G. M. Ziarani, A. Habibi-Yangjeh, M. J. Munoz-Batista and R. Luque, Graphitic carbon nitride-based photocatalysts: Toward efficient organic transformation for value-added chemicals production, *Mol. Catal.*, 2020, **488**, 110902.
8 C. F. Huang, Y. P. Wen, J. Ma, D. D. Dong, Y. F. Shen, S. Q. Liu, H. B. Ma and Y. J. Zhang, Unraveling fundamental active units in carbon nitride for photocatalytic oxidation reactions, *Nat. Commun.*, 2021, **12**, 320.
9 D. M. Zhao, Y. Q. Wang, C. L. Dong, Y. C. Huang, J. Chen, F. Xue, S. H. Shen and L. J. Guo, Boron-doped nitrogen-deficient carbon nitride-based *Z*-scheme heterostructures for photocatalytic overall water splitting, *Nat. Energy*, 2021, **6**, 388–397.
10 S. W. Cao, J. X. Low, J. G. Yu and M. Jaroniec, Polymeric photocatalysts based on graphitic carbon nitride, *Adv. Mater.*, 2015, **27**, 2150–2176.
11 J. Li, D. D. Wu, J. Iocozzia, H. W. Du, X. Q. Liu, Y. P. Yuan, W. Zhou, Z. Li, Z. M. Xue and Z. Q. Lin, Achieving efficient incorporation of π-electrons into graphitic carbon nitride for markedly improved hydrogen generation, *Angew. Chem., Int. Ed.*, 2019, **58**, 1985–1989.
12 Y. Zou, K. Xiao, Q. Qin, J. W. Shi, T. Heil, Y. Markushyna, L. Jiang, M. Antonietti and A. Savateev, Enhanced organic photocatalysis in confined flow through a carbon nitride nanotube membrane with conversions in the millisecond regime, *ACS Nano*, 2021, **15**, 6551–6561.
13 Y. Lv, D. Ma, K. Song, S. Mao, Z. Liu, D. He, X. Zhao, T. Yao and J. W. Shi, Graphitic carbon nitride decorated with C–N compounds broken by *s*-triazine unit as homojunction for photocatalytic $H_2$ evolution, *J. Mater. Chem. A*, 2023, **11**, 800–808.
14 J. Zhang, G. Ye, C. Zhang, Z. Pan, S. Wang, G. Zhang and X. Wang, Heptazine-based ordered-distorted copolymers with enhanced visible-light absorption for photocatalytic hydrogen production, *ChemSusChem*, 2022, **15**, e202201616.
15 J. Zhang, X. Liang, C. Zhang, L. Lin, W. Xing, Z. Yu, G. Zhang and X. Wang, Improved charge separation in poly(heptazine-triazine) imides with semi-coherent interfaces for photocatalytic hydrogen evolution, *Angew. Chem., Int. Ed.*, 2022, **61**, e202210849.
16 H. Li, L. P. Wang and G. Yu, Covalent organic frameworks: Design, synthesis, and performance for photocatalytic applications, *Nano Today*, 2021, **40**, 101247.
17 S. Karak, V. Stepanenko, M. A. Addicoat, P. Kessler, S. Moser, F. Beuerle and F. Wurthner, A Covalent organic framework for cooperative water oxidation, *J. Am. Chem. Soc.*, 2022, **144**, 17661–17670.
18 T. Banerjee, F. Podjaski, J. Kroger, B. P. Biswal and B. V. Lotsch, Polymer photocatalysts for solar-to-chemical energy conversion, *Nat. Rev. Mater.*, 2021, **6**, 168–190.
19 X. Y. Wang, L. J. Chen, S. Y. Chong, M. A. Little, Y. Z. Wu, W. H. Zhu, R. Clowes, Y. Yan, M. A. Zwijnenburg, R. S. Sprick and A. I. Cooper, Sulfone-containing covalent organic frameworks for photocatalytic hydrogen evolution from water, *Nat. Chem.*, 2018, **10**, 1180–1189.
20 H. Wang, H. Wang, Z. W. Wang, L. Tang, G. M. Zeng, P. Xu, M. Chen, T. Xiong, C. Y. Zhou, X. Y. Li, D. N. Huang, Y. Zhu, Z. X. Wang and J. W. Tang, Covalent organic framework photocatalysts: structures and applications, *Chem. Soc. Rev.*, 2020, **49**, 4135–4165.
21 Z. F. Qian, Z. J. Wang and K. A. I. Zhang, Covalent triazine frameworks as emerging heterogeneous photocatalysts, *Chem. Mater.*, 2021, **33**, 1909–1926.
22 K. W. Wang, L. M. Yang, X. Wang, L. P. Guo, G. Cheng, C. Zhang, S. B. Jin, B. Tan and A. Cooper, Covalent triazine frameworks *via* a low-temperature polycondensation approach, *Angew. Chem., Int. Ed.*, 2017, **56**, 14149–14153.
23 W. Huang, Q. He, Y. P. Hu and Y. G. Li, Molecular heterostructures of covalent triazine frameworks for enhanced photocatalytic hydrogen production, *Angew. Chem., Int. Ed.*, 2019, **58**, 8676–8680.
24 Z. A. Lan, M. Wu, Z. P. Fang, Y. F. Zhang, X. Chen, G. G. Zhang and X. C. Wang, Ionothermal synthesis of covalent triazine frameworks in a NaCl-KCl-$ZnCl_2$ eutectic salt for the hydrogen evolution reaction, *Angew. Chem., Int. Ed.*, 2022, **61**, e202201482.
25 M. Liu, C. Wei, H. Zhuzhang, J. Zhou, Z. Pan, W. Lin, Z. Yu, G. Zhang and X. Wang, Fully condensed poly(triazine imide) crystals: Extended π-conjugation and structural defects for overall water splitting, *Angew. Chem., Int. Ed.*, 2022, **61**, e202113389.
26 M. Barawi, L. Collado, M. Gomez-Mendoza, F. E. Oropeza, M. Liras and V. A. P. O'Shea, Conjugated porous polymers: ground-breaking materials for solar energy conversion, *Adv. Energy Mater.*, 2021, **11**, 2101530.
27 L. Yang, Y. T. Peng, X. D. Luo, Y. Dan, J. H. Ye, Y. Zhou and Z. G. Zou, Beyond $C_3N_4$ π-conjugated metal-free polymeric semiconductors for photocatalytic chemical transformations, *Chem. Soc. Rev.*, 2021, **50**, 2147–2172.
28 S. H. Luo, Z. T. Zeng, G. M. Zeng, Z. F. Liu, R. Xiao, P. Xu, H. Wang, D. L. Huang, Y. Liu, B. B. Shao, Q. H. Liang, D. B. Wang, Q. Y. He, L. Qin and Y. K. Fu, Recent advances in conjugated microporous polymers for photocatalysis:

designs, applications, and prospects, *J. Mater. Chem. A*, 2020, **8**, 6434–6470.

29 C. Shu, C. Z. Han, X. Y. Yang, C. Zhang, Y. Chen, S. J. Ren, F. Wang, F. Huang and J. X. Jiang, Boosting the photocatalytic hydrogen evolution activity for D–π–A conjugated microporous polymers by statistical copolymerization, *Adv. Mater.*, 2021, **33**, 2008498.

30 S. Chu, Y. Wang, Y. Guo, P. Zhou, H. Yu, L. Luo, F. Kong and Z. Zou, Facile green synthesis of crystalline polyimide photocatalyst for hydrogen generation from water, *J. Mater. Chem.*, 2012, **22**, 15519.

31 S. Chu, Y. Wang, C. C. Wang, J. C. Yang and Z. G. Zou, Bandgap modulation of polyimide photocatalyst for optimum $H_2$ production activity under visible light irradiation, *Int. J. Hydrogen Energy*, 2013, **38**, 10768–10772.

32 S. Chu, Y. Y. Pan, Y. Wang, H. Y. Zhang, R. Xiao and Z. G. Zou, Polyimide-based photocatalysts: rational design for energy and environmental applications, *J. Mater. Chem. A*, 2020, **8**, 14441–14462.

33 C. C. Wang, Y. Guo, Y. Yang, S. Chu, C. K. Zhou, Y. Wang and Z. G. Zou, Sulfur-doped polyimide photocatalyst with enhanced photocatalytic activity under visible light irradiation, *ACS Appl. Mater. Interfaces*, 2014, **6**, 4321–4328.

34 Z. W. Cui, J. Zhou, T. Liu, Y. C. Wang, Y. Hu, Y. Wang and Z. G. Zou, Porphyrin-containing polyimide with enhanced light absorption and photocatalysis activity, *Chem. – Asian J.*, 2019, **14**, 2138–2148.

35 K. L. Zhang, H. M. Li, H. X. Shi and W. Hong, Polyimide with enhanced π stacking for efficient visible-light-driven photocatalysis, *Catal. Sci. Technol.*, 2021, **11**, 4889–4897.

36 S. Chu, C. C. Wang, Y. Yang, Y. Wang and Z. G. Zou, Developing high-efficiency π conjugated polymer semiconductor for photocatalytic degradation of dyes under visible light irradiation, *RSC Adv.*, 2014, **4**, 57153–57158.

37 H. M. Heng, J. P. Yang, Y. J. Yin, P. C. Meng and X. Liu, Effect of precursor types on the performance of polyimide: A metal-free visible-light-driven photocatalyst for effective photocatalytic degradation of pollutants, *Catal. Today*, 2020, **340**, 225–235.

38 X. T. Wang, S. Chu, J. J. Shao, C. Liu, Z. C. Luo, R. Xiao and H. Y. Zhang, Efficient and selective C-C bond cleavage of a lignin model using a polyimide photocatalyst with high photooxidation capability, *ACS Sustainable Chem. Eng.*, 2022, **10**, 11555–11566.

39 Y. Huang, Q. Wang, J. L. Zhang, Y. Y. Yu, Y. Dan and L. Jiang, Better choice for a polyimide photocatalyst: planar or stereo crosslinked structures?, *Ind. Eng. Chem. Res.*, 2022, **61**, 8752–8762.

40 J. Zhou, Y. C. Wang, Z. W. Cui, Y. Hu, X. Q. Hao, Y. Wang and Z. G. Zou, Ultrathin conjugated polymer nanosheets as highly efficient photocatalyst for visible light driven oxygen activation, *Appl. Catal., B*, 2020, **277**, 119228.

41 J. Zhou, Y. C. Wang, X. Q. Hao, C. H. Ma, Y. Wang and Z. H. Zou, Controllable conformation transfer of conjugated polymer toward high photoelectrical performance: the role of solvent in induced-crystallization route, *J. Phys. Chem. C*, 2018, **122**, 1037–1043.

42 X. F. Zhao, X. B. Yi, X. Q. Wang, J. Zhang, B. X. Liu, X. C. Liu, S. P. Guo and W. Chu, Highly efficient visible-light-induced photoactivity of carbonized polyimide aerogel for antibiotic degradation, *Nanotechnology*, 2020, **31**, 235707.

43 W. L. Sheng, J. L. Shi, H. M. Hao, X. Li and X. J. Lang, Polyimide-$TiO_2$ hybrid photocatalysis: Visible light-promoted selective aerobic oxidation of amines, *Chem. Eng. J.*, 2020, **379**, 122399.

44 S. Q. Chu, Y. Hu, J. Zhang, Z. W. Cui, J. Y. Shi, Y. Wang and Z. G. Zou, Constructing direct *Z*-scheme CuO/PI heterojunction for photocatalytic hydrogen evolution from water under solar driven, *Int. J. Hydrogen Energy*, 2021, **46**, 9064–9076.

45 C. H. Ma, J. Zhou, H. Y. Zhu, W. W. Yang, J. G. Liu, Y. Wang and Z. G. Zou, Constructing a high-efficiency $MoO_3$/polyimide hybrid photocatalyst based on strong interfacial interaction, *ACS Appl. Mater. Interfaces*, 2015, **7**, 14628–14637.

46 X. Y. Huang and X. Liu, Highly polymerized linear polyimide/$H_3PW_{12}O_{40}$ photocatalyst with full visible light region absorption, *Chemosphere*, 2021, **283**, 131230.

47 J. Y. Li, X. Jiang, L. Lin, J. J. Zhou, G. S. Xu and Y. P. Yuan, Improving the photocatalytic performance of polyimide by constructing an inorganic–organic hybrid ZnO-polyimide core-shell structure, *J. Mol. Catal. A: Chem.*, 2015, **406**, 46–50.

48 C. H. Ma, M. Y. Jiang, C. Q. Yang, Z. A. Yang, W. Meng, L. Zhou, C. Y. Sun and W. Q. Chen, Construction of α-$Fe_2O_3$/sulfur-doped polyimide direct *Z*-scheme photocatalyst with enhanced solar light photocatalytic activity, *ACS Omega*, 2022, **7**, 11371–11381.

49 Y. Hu, X. Q. Hao, Z. W. Cui, J. Zhou, S. Q. Chu, Y. Wang and Z. G. Zou, Enhanced photocarrier separation in conjugated polymer engineered CdS for direct *Z*-scheme photocatalytic hydrogen evolution, *Appl. Catal., B*, 2020, **260**, 118131.

50 H. X. Deng, J. W. Luo and S. H. Wei, Band structure engineering and defect control of oxides for energy applications, *Chin. Phys. B*, 2018, **27**, 117104.

51 Z. C. Xiao, X. X. Huang, K. Zhao, Q. Song, R. Y. Guo, X. H. Zhang, S. K. Zhou, D. B. Kong, M. Wagner, K. Mullen and L. J. Zhi, Band structure engineering of Schiff-base microporous organic polymers for enhanced visible-light photocatalytic performance, *Small*, 2019, **15**, 1900244.

52 Y. Q. Xiao, C. Feng, J. Fu, F. Z. Wang, C. L. Li, V. F. Kunzelmann, C. M. Jiang, M. Nakabayashi, N. Shibata, I. D. Sharp, K. Domen and Y. B. Li, Band structure engineering and defect control of $Ta_3N_5$ for efficient photoelectrochemical water oxidation, *Nat. Catal.*, 2020, **3**, 932–940.

53 Y. X. Fang, Y. D. Hou, X. Z. Fu and X. C. Wang, Semiconducting polymers for oxygen evolution reaction under light illumination, *Chem. Rev.*, 2022, **122**, 4204–4256.

54 J. Zhang, Z. J. Wang, J. Y. Shi, W. B. Zhu, L. Yang, Y. Wang and Z. G. Zou, Bay-monosubstitution with electron-donating group as an efficiently strategy to functionalize perylene imide polymer for enhancing photocatalytic oxygen evolution activity, *Adv. Funct. Mater.*, 2022, **32**, 2205895.

55 D. C. Xie, Y. T. Li, H. A. Dong, W. J. Jing, Y. X. Liu, F. Y. Wu, J. W. Zhang and Z. Zhang, Key role of valence band position

in porous carbon nitride for photocatalytic water splitting, *J. Phys. Chem. C*, 2022, **126**, 14173–14179.

56 H. Zhao, Y. F. Dong, P. Y. Sun, Y. F. Bai, C. L. Ru, X. Wu, Z. H. Li, X. N. Han, J. C. Wu and X. B. Pan, Effect of D/A ratio on photocatalytic hydrogen evolution performance of conjugated polymer photocatalysts, *ACS Appl. Energy Mater.*, 2022, **5**, 4631–4640.

57 Q. Zhang, J. Chen, H. A. Che, P. F. Wang, B. Liu and Y. H. Ao, Recent advances in g-$C_3N_4$-based donor-acceptor photocatalysts for photocatalytic hydrogen evolution: An exquisite molecular structure engineering, *ACS Mater. Lett.*, 2022, **4**, 2166–2186.

58 C. Z. Han, S. H. Xiang, P. X. Xie, P. H. Dong, C. Shu, C. Zhang and J. X. Jiang, A universal strategy for boosting hydrogen evolution activity of polymer photocatalysts under visible light by inserting a narrow-band-gap spacer between donor and acceptor, *Adv. Funct. Mater.*, 2022, **32**, 2109423.

59 G. F. Liao, C. X. Li and B. Z. Fang, Donor-acceptor organic semiconductor heterojunction nanoparticles for efficient photocatalytic $H_2$ evolution, *Matter*, 2022, **5**, 1635–1637.

60 Z. A. Lan, Y. Fang, Y. Zhang and X. Wang, Photocatalytic oxygen evolution from functional triazine-based polymers with tunable band structures, *Angew. Chem., Int. Ed.*, 2018, **57**, 470–474.

61 L. Wang, W. Huang, R. Li, D. Gehrig, P. W. M. Blom, K. Landfester and K. A. I. Zhang, Structural design principle of small-molecule organic semiconductors for metal-free, visible-light-promoted photocatalysis, *Angew. Chem., Int. Ed.*, 2016, **55**, 9783–9787.

62 Y. P. Wang, G. P. Ji, W. Q. Ye, F. T. Zhang, Y. D. Wang, Y. F. Zhao and Z. M. Liu, DFT-assisted design of D-A conjugated polymers for photocatalytic reduction of carbon dioxide, *ACS Sustainable Chem. Eng.*, 2022, **10**, 9460–9468.

63 P. Kong, H. Tan, T. Y. Lei, J. Wang, W. J. Yan, R. Y. Wang, E. R. Waclawik, Z. F. Zheng and Z. Li, Oxygen vacancies confined in conjugated polyimide for promoted visible-light photocatalytic oxidative coupling of amines, *Appl. Catal., B*, 2020, **272**, 118964.

64 S. Chu, Y. Wang, Y. Guo, J. Feng, C. Wang, W. Luo, X. Fan and Z. Zou, Band structure engineering of carbon nitride: In search of a polymer photocatalyst with high photooxidation property, *ACS Catal.*, 2013, **3**, 912–919.

65 Y. Shiraishi, S. Kanazawa, Y. Kofuji, H. Sakamoto, S. Ichikawa, S. Tanaka and T. Hirai, Sunlight-driven hydrogen peroxide production from water and molecular oxygen by metal-free photocatalysts, *Angew. Chem., Int. Ed.*, 2014, **53**, 13454–13459.

66 J. H. Park, A. Soon and J. H. Lee, A computational survey of metal-free polyimide-based photocatalysts within the single-stranded polymer model, *Mol. Catal.*, 2020, **497**, 111184.

67 A. W. Prentice and M. A. Zwijnenburg, The role of computational chemistry in discovering and understanding organic photocatalysts for renewable fuel synthesis, *Adv. Energy Mater.*, 2021, **11**, 2100709.

68 P. Meng, H. Heng, Y. Sun, J. Huang, J. Yang and X. Liu, Positive effects of phosphotungstic acid on the in-situ solid-state polymerization and visible light photocatalytic activity of polyimide-based photocatalyst, *Appl. Catal., B*, 2018, **226**, 487–498.

69 P. Liu, N. Sun, Y. Liang and F. Chen, Modified graphitic carbon nitride prepared *via* a copolymerization route for superior photocatalytic activity, *Res. Chem. Intermed.*, 2017, **44**, 843–857.